High-Efficiency Mid-Range Inductive Power Transfer Employing Alternative-Winding Coils

Zixuan Yi, Meiling Li, Badar Muneer, *Member, IEEE*, and Qi Zhu

***Abstract*—A novel coil with alternative clockwise and counterclockwise winding has been proposed and employed to construct inductive power transfer (IPT) systems. After establishing the equivalent circuit of the proposed IPT system, the coil-to-coil, source-to-load, and optimum transfer efficiency are analyzed mathematically. Then, comprehensive expressions for accurate estimation of transfer efficiency of a realizable structure are deduced. Theoretical analyses indicate that it is not always mandatory to use extremely low-loss material to fabricate the coils for high-efficiency mid-range wireless power transfer (WPT) systems. To validate the proposed IPT system, a prototype is designed, fabricated, and measured. Good agreements are achieved between calculated and experimental results. It is demonstrated that the adoption of the present coil can enhance the IPT systems' performance significantly. Compared with traditional IPT systems, the present system can operate properly without surplus and complex compensating networks. Further, an IPT system at 13.56 MHz employing proposed coils without any matching networks is designed, fabricated, and tested. This system is then used to drive a LED monitor wirelessly to demonstrate the feasibility of the proposed system in commercial applications. Owing to its design simplicity and demonstrated benefits, the proposed configuration endeavors to replace traditional approach to design high-efficiency optimized WPT systems.**

***Index Terms*—Coils, electromagnetic induction, inductive power transfer (IPT), mutual coupling, power transmission, wireless power transfer (WPT).**

I. Introduction

WIRELESS power transfer (WPT) technologies have attracted an increased attention in recent years. Researches on WPT mainly focus on electromagnetic fields. According to power transfer manner, WPT can be realized through radiative or nonradiative methods. The radiative technique, comprising optical power transfer and microwave power transfer [1]–[3], can transfer energy to a relatively far

Manuscript received March 26, 2018; revised June 2, 2018 and August 14, 2018; accepted September 16, 2018. Date of publication September 23, 2018; date of current version May 2, 2019. This work was supported by the Higher Education Commission of Pakistan under Grant NRPU/6876. Recommended for publication by Associate Editor O. C. Onar. *(Corresponding author: Qi Zhu.)*

Z. Yi, M. Li, and Q. Zhu are with the Electrical Engineering and Information Science Department, University of Science and Technology of China, Hefei 230026, China (e-mail:

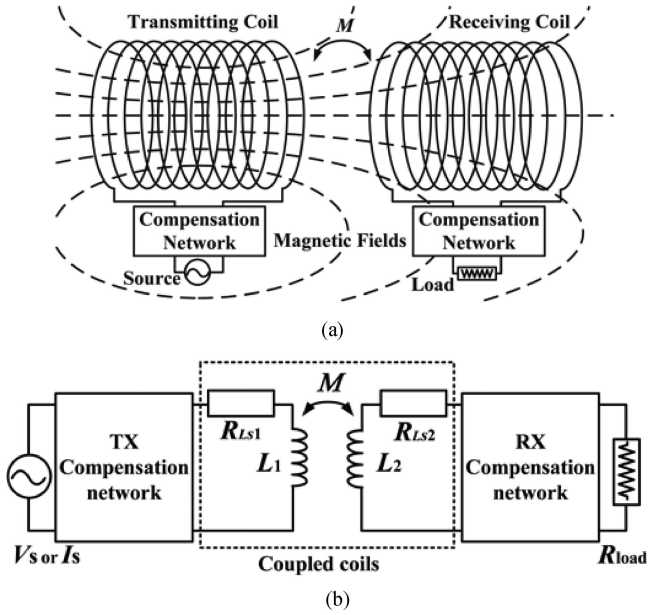

Fig. 1. Traditional IPT. (a) Sketch of two coils without magnetic cores. (b) Equivalent circuit model of traditional IPT [21].

detailed equivalent circuit is developed and analyzed. All the parameters in equivalent circuit can be derived directly from the geometrical structure and material constants of the IPT configurations. Moreover, it is also possible to deduce the transfer efficiency directly from the equivalent circuit model without involving unnecessary estimation of electrical parameters. Finally, a pair of proposed AWCs is designed and manufactured. It has been demonstrated that with the same coil size, the proposed IPT system with AWC (with proper scaling) can achieve longer range and better power transfer efficiency. The measured results reveal that the present IPT configuration can achieve the transfer range of 6 times the coil diameter with 50% of transfer efficiency, validating the analytical and theoretical results. According to the analysis, longer transfer range can be achieved by increasing the number of turns provided that the wire properties are kept constant.

II. Traditional IPT Model and Discussion on Power Transfer Efficiency

A. Traditional IPT Structure and Equivalent Circuit

A typical traditional IPT system is basically composed of a signal source, a transmitting (TX) coil, a receiving (RX) coil, compensation networks, and a load, as shown in Fig. 1(a). Fig. 1(b) shows the equivalent circuit model of the two-coil IPT system. An equivalent ac voltage source or current source is adopted as the power supply. $R_{\rm load}$ is the equivalent loading resistance, $R_{\rm Ls1}$ and $R_{\rm Ls2}$ are the resistances of the TX and RX coils, respectively. L_1 and L_2 are the self-inductance of TX and RX, whereas *M* is the mutual inductance of TX and RX. The compensation network with series or parallel compensators is used to compensate the imaginary part induced by the coil [19]–[21].

B. Discussion of Power Transfer Efficiency

Majorly, there are four factors influencing the power transfer efficiency, the operating frequency, the mutual inductance, the loss of coils, and source/load impedance matching of the system.

The first factor is the working frequency of coils. According to Faraday's law of electromagnetic induction, the mutual effects between TX coil and RX coil can be described by the induced electromotive forces e_{21} and e_{12}, respectively. Under the excitation of harmonic wave with an angular frequency ω, the induced electromotive force can be expressed as

$$e_{21} = M_{21}\frac{di_1}{dt} = -j\omega M_{21} i_1 \tag{1}$$

$$e_{12} = M_{12}\frac{di_2}{dt} = -j\omega M_{12} i_2 \tag{2}$$

where $M_{12} = M_{21} = M$ represents the mutual inductance between TX and RX coil. i_1 and i_2 are the currents in TX coil and RX coil, respectively. It can be concluded from the basic theory of IPT that there is a positive correlation between the transfer efficiency and the factor ωM [22]. In other words, the transfer efficiency of IPT system operating at high frequency is higher than that of a system operating at low frequency with the same mutual inductances and losses.

Besides the key roles of geometry and the relative position of coils on the mutual inductance [23], the current distribution on the coil has a remarkable effect on the mutual inductance especially at high frequencies, which is always unfortunately overlooked. In this paper, the importance of current distribution is highlighted and discussed in detail in later sections. In Fig. 1(a), the magnetic flux in RX coil is determined by the magnetic field of TX coil, which is further determined by the current distribution of TX coil. The mutual inductance M_{21} is defined as the magnetic flux Φ_{21} through RX coil generated by per unit current i_1 of the TX coil [24], shown as follows:

$$M_{21} = \Phi_{21}\left(s_2, i_1\right)/i_1. \tag{3}$$

Ideally, to achieve the optimum mutual inductance requires that the currents in each loop of coil flow in the same direction and remain in-phase.

The loss of coils has a certain effect on the transfer efficiency. The higher the loss, the lower the transfer efficiency will be [8]–[14]. Finally, the source and load impedance should be well matched to the system in order to avoid reflection. Commonly, the compensating networks with parallel/series capacitors are used to minimize the mismatch [19]–[21].

Often, low frequencies (generally below 100 kHz) are chosen as operating frequency of a traditional IPT system [20]. This is due to the fact that the phase and direction of the current of each loop could be considered approximately the same at low frequencies, while the coils working at lower frequencies possess lower loss. It seems that with the later three requirements satisfied, the efficiency of midrange inductive coupled coils could be improved by increasing the operating frequency. In reality, increasing of operating frequency alone cannot get a proper IPT system with good transfer efficiency due to the following reasons. First, the input impedance of coil varies violently at high

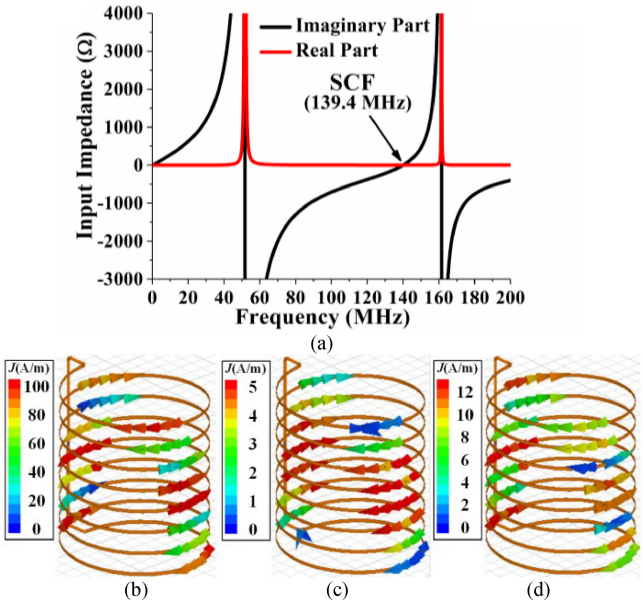

Fig. 2. Characteristics of a conventional eight-turn coil without magnetic cores. (a) Input impedance as a function of frequency. Maximum amplitude current distributions at (b) the short circuit frequency at 90° (scale: 0–100 A/m), (c) the first-order resonant frequency at 180° (scale: 0–5 A/m), and (d) the second-order resonant frequency at 180° (scale: 0–13 A/m).

frequencies. Second, the decreased wavelength let the currents along different loops be out of phase even in different directions. Third, the ohmic loss increases with the operating frequency.

To check the effects of frequency on the efficiency of midrange inductive coupled coils, an eight-turn traditional coil is taken as an example to investigate the frequency dependence of input impedance and current distribution. Fig. 2(a) shows the simulated input impedance of a lossless eight-turn coil with coil diameter, length, and wire diameter of 0.1, 0.12, and 0.002 m respectively. The resonant frequencies of the first and second order are 51.8 and 162 MHz, respectively. Fig. 2(b)–(d) shows the simulated current distributions at different frequencies. It can be seen that the currents along different loops are out of phase even in different directions.

The physical reason of the current behavior in Fig. 2 can be expressed as follows: when the operating frequency gets higher, the wavelength gets shorter. When the wavelength is comparable with the coil length, the current along different turns cannot keep pace with each other. The current distribution can be derived from a time-domain analysis.

Suppose that a sinusoidal source $u_{\text{in}} = U_0 \sin(\omega t)$ is applied to both the ends [points A and B in Fig. 3(a)] of the coil wire. Straighten the coil and place it along the x-axis, as shown in Fig. 3(b). Let C be an arbitrary point between A and B, the voltage and current at point C can be expressed as

$$u_c = \frac{U_0}{2} e^{j(\omega t - k x_c)} - \frac{U_0}{2} e^{j(\omega t - k(l_w - x_c))} \tag{4}$$

$$i_c = \frac{I_0}{2} e^{j(\omega t - k x_c)} + \frac{I_0}{2} e^{j(\omega t - k(l_w - x_c))} \tag{5}$$

where x_c is the distance between points A and C, l_w is the total length of the wire, and $k = 2\pi f/c$ is the wave vector. In (4), the

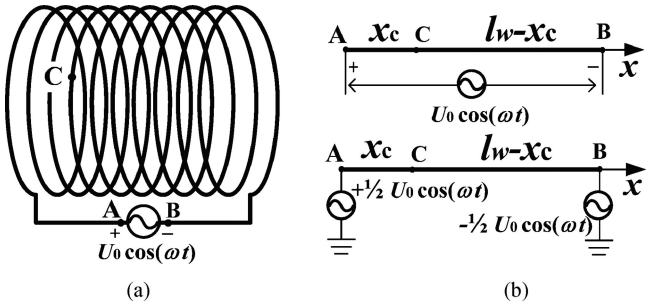

Fig. 3. (a) Schematic diagram of solenoidal coil. (b) Coordinate x along the wire.

first and second terms represent the voltage wave propagating from A→C and B→C, respectively, whereas in (5), the terms represent currents from A→C and B→C, respectively.

The voltages and currents at points A and B are given as follows:

$$u_A = \frac{U_0}{2} e^{j\omega t} - \frac{U_0}{2} e^{j(\omega t - k l_w)} \tag{6}$$

$$i_A = \frac{I_0}{2} e^{j\omega t} + \frac{I_0}{2} e^{j(\omega t - k l_w)} \tag{7}$$

$$u_B = \frac{U_0}{2} e^{j(\omega t - k l_w)} - \frac{U_0}{2} e^{j\omega t} \tag{8}$$

$$i_B = \frac{I_0}{2} e^{j(\omega t - k l_w)} + \frac{I_0}{2} e^{j\omega t}. \tag{9}$$

Thus, the input impedance Z_{in} can be calculated as

$$Z_{\text{in}} = \frac{u_A - u_B}{i_A + i_B} = \frac{U_0 \left[1 - e^{-j\frac{2\pi l_w}{\lambda}}\right]}{I_0 \left[1 + e^{-j\frac{2\pi l_w}{\lambda}}\right]}. \tag{10}$$

Theoretically, the imaginary part of input impedance at short-circuit frequency (SCF) reaches zero, whereas at resonant frequency it reaches the infinity. Thus, (11) and (12) which make imaginary part of (10) to be 0 and ∞ are the short-circuit condition and resonance condition, respectively.

$$l_w = n_i \lambda \qquad (n_i = 1, 2, 3 \ldots) \tag{11}$$

$$l_w = \frac{2n_j - 1}{2} \lambda \qquad (n_j = 1, 2, 3 \ldots) \tag{12}$$

where n_i and n_j represent the ith SCF and jth resonance frequency, respectively.

By putting (11) into (5), the current distribution $i_{x,t}$ along the coil wire at SCF can be expressed as

$$i_{x,t} = I_0 \cos\left(\frac{2n_i \pi x}{l_w}\right) e^{j\omega t} \qquad (n_i = 1, 2, 3 \ldots). \tag{13}$$

In the same way, the current distribution at resonance frequency is

$$i_{x,t} = I_0 \sin\left(\frac{(2n_j - 1)\pi x}{l_w}\right) e^{j(\omega t - \pi/2)} \qquad (n_j = 1, 2, 3 \ldots). \tag{14}$$

Therefore, the current distributions along the wire shown in Fig. 2 can be described and explained by (13) and (14).

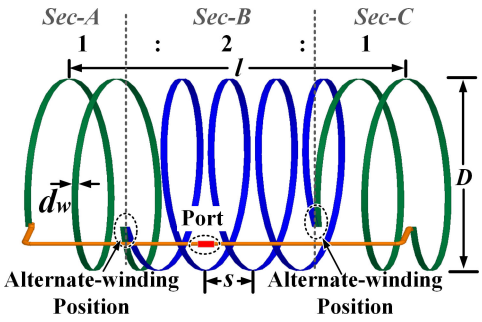

Fig. 4. Proposed AWC. The parameters D, l, d_w, and l_w are coil diameter, coil length, wire diameter, and total wire length, respectively. s is the distance between the centers of two adjacent loops.

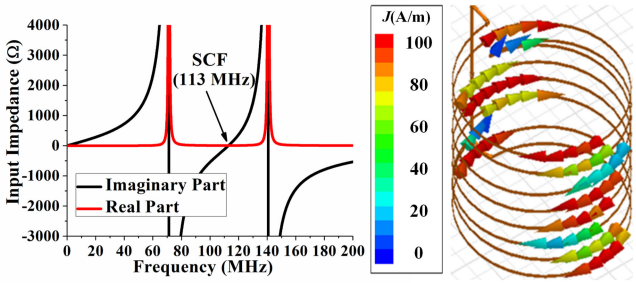

Fig. 5. Characteristics of the eight-turn AWC. (a) Input impedance as a function of frequency. (b) Maximum amplitude current distribution at SCF of 113 MHz (scale: 0–100 A/m).

III. Proposed Coil and Corresponding IPT Structure

A. Proposed Coil Structure for High-Frequency IPT

Though there are troubles to employing coils in IPT at high frequencies, a noteworthy frequency is found between two resonant frequencies at 139.4 MHz, as shown in Fig. 2(a). The impedance at the frequency is similar to that of a short circuit because the imaginary and real parts are approximately equal to zero. This frequency point is termed as SCF in the rest of the paper. At SCF, the coil can be matched to the source/load directly, completely eliminating the surplus compensating network. However, the directions of currents at both ends of the coil at SCF are opposite to the middle section, as highlighted in Fig. 2(b). It makes the magnetic fields to interfere destructively instead of constructively, causing the recession in mutual inductance.

To benefit from the advantages of coil at SCF while avoiding the magnetic fields recession, an AWC structure is proposed here that can address the issue of asynchronous current directions. The scheme of coil is shown in Fig. 4. The coil is divided into three sections with the middle section always having the direction of winding reversed with respect to the two ends. By simulating different coils with different number of turns, the behavior of coils is studied. A plentiful study revealed that the proper turn ratio for the three sections of AWC is 1:2:1, which has also been proven theoretically below.

The input impedance of an eight-turn AWC simulated using commercially available software is shown in Fig. 5(a). The parameters D, l, d_w, and l_w are 0.1, 0.12, 0.002, and 2.63 m,

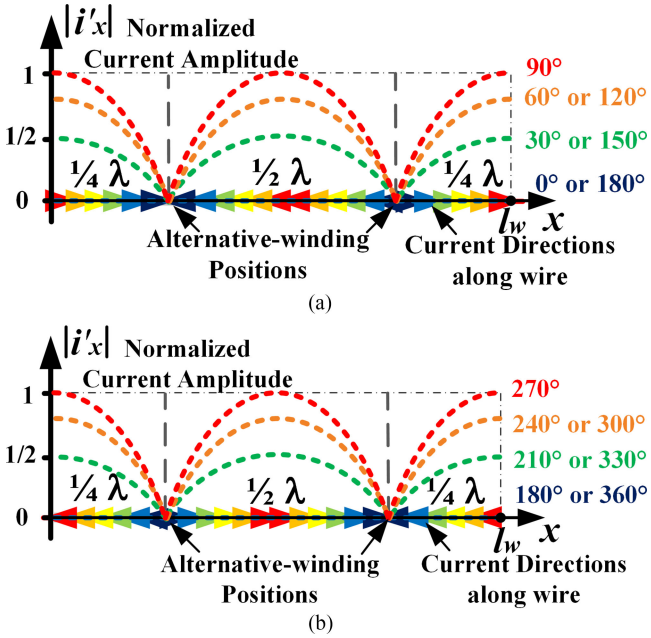

Fig. 6. Distribution of standing-wave current along the wire of the coil at SCF. (a) Phase interval of sinusoidal source (0, 180). (b) Phase interval of sinusoidal source (180, 360). The current directions are opposite in (a) and (b).

respectively. The first and second resonant frequencies are 71.2 and 141 MHz, respectively.

The current distribution at SCF (113 MHz in this case) is shown in Fig. 5(b), which shows the currents rotation in each section is unidirectional and in-phase. Besides the directions of the current flow, the current amplitude along the wire influences the ohmic loss and mutual inductance of coils.

Fig. 6 shows the normalized simulated current amplitudes along the straightened coil at SCF for sinusoidal source excitation with different phases. According to Fig. 5, the normalized current distribution $i'_{x,t}$ along the wire can be expressed as follows:

$$\left|i'_{x,t}\right| = \left|i_{x,t}/I_0\right| = \left|\sin(\omega t)\cos\left(\frac{2\pi x}{l_w}\right)\right|, x \in [0, l_w] \quad (15)$$

where $i_{x,t}$ and I_0 is the current distribution along the wire and maximum current amplitude on the wire, respectively. Both Fig. 6 and (15) reveal that the lengths of three segments of wires with a perpetual current direction are $1/4$, $1/2$, and $1/4$ wavelength, respectively, which explain the proper turn ratio of 1:2:1.

For illustrating the superiority of the AWC at SCF, magnetic field strengths generated by traditional coil and the proposed coil are given. Fig. 7 shows the comparison of magnetic field strengths along the coil axis. It can be found that the proposed coil at SCF has maximum field strength, even at the farther most point along z-axis. The dip in the field strength curve of the traditional coil at SCF is caused by destructive interference due to opposite current directions, whereas the proposed coil maintains the field strength by making the currents unidirectional all along the coil. The same phenomenon can also be observed in Fig. 8(d).

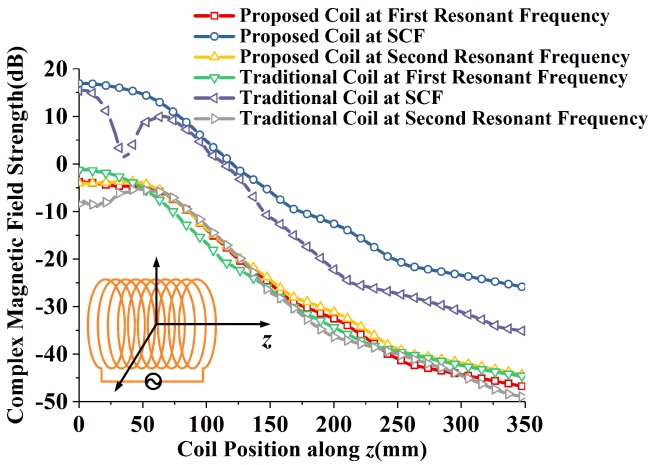

Fig. 7. Complex magnetic field strength variation along the z-axis. The operating frequencies and coil current levels correspond to the values shown in Figs. 2 and 5.

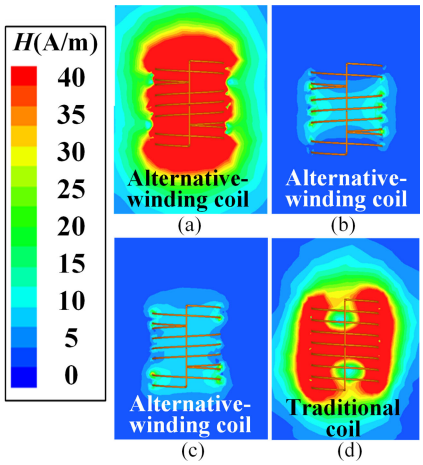

Fig. 8. Complex magnetic field strength distributions. The scale ranges of fields are the same (a) at the SCF (113 MHz) of AWC, (b) at the first-order resonant frequency of 71.2 MHz, (c) at the second-order resonant frequency of 141 MHz, and (d) at the SCF (139.4 MHz) of traditional coil.

Fig. 8(a)–(c) shows the distributions of complex magnetic field strength of the eight-turn AWC at 113, 71.2, and 141 MHz, respectively. Fig. 8(d) shows the field distribution of an eight-turn conventional coil of the same size at SCF (139.4 MHz).

B. AWCs With 2n Flips

Through a similar process, the analysis is extended to use coils of length $n\lambda$ with $2n$ rotational flips at positions $(2 \cdot i + 1) \cdot \lambda/4$, $i = 0, 1, ..., 2n-1$. The simulated and analyzed results reveal that their real and imaginary part of input impedance are minimum and zero, respectively, which make the currents at both ends of the coil reach its maximum value and remain in-phase. In other words, the standing-wave current distribution along the coil is ended with crests at both ends. Thus, the total length of AWCs with $2n$ rotational flips is $n\lambda$, and the turn ratio is $1 : \underbrace{2 : \cdots : 2 : \cdots : 2}_{2n-1} : 1$. Fig. 9 shows the normalized current distribution of AWCs with $n = 1, 2, 3$

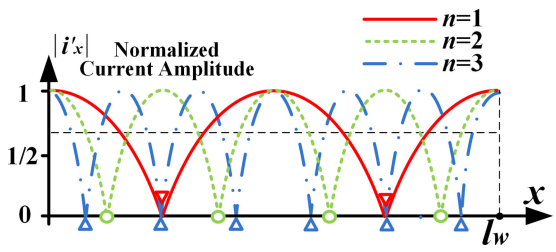

Fig. 9. Distribution of standing-wave current along the wire of AWCs with $n = 1, 2, 3$. The alternative-winding positions are marked by corresponding makers.

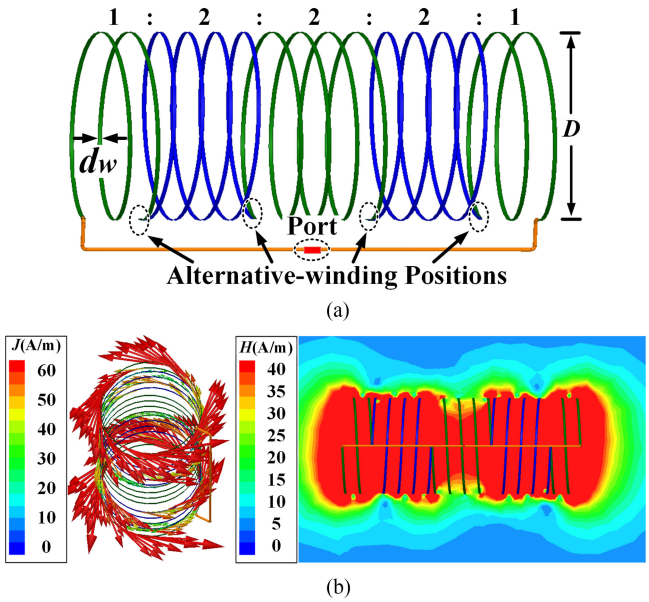

Fig. 10. AWC of $n = 2$. (a) Structure. (b) Current along the wire. (c) Complex magnetic field strength distributions.

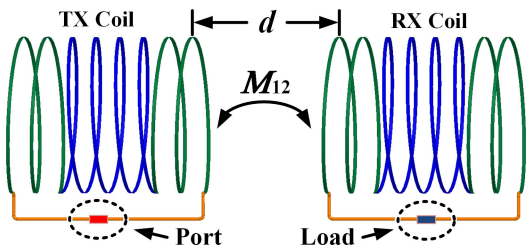

Fig. 11. Scheme of an IPT system employing two AWCs.

and the alternative-winding positions are marked in the figure. Fig. 10(b) shows the current along the wire for AWC with $n = 2$. By the way, it is difficult to properly visualize the current vector distributions of more turn due to over congestion of current vectors.

C. IPT System Employing Proposed Coils

The IPT system employing two identical co-axial AWCs is shown in Fig. 11. The end-to-end coil distance is d, this distance is also the transfer distance. The factor M_{12} is the coefficient of mutual induction. The TX coil is connected to a signal generator

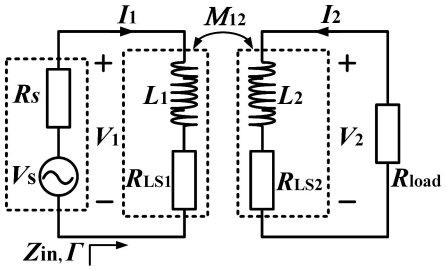

Fig. 12. Equivalent circuit model of the proposed IPT system employing AWCs. The coil is modeled as a special inductor in series with a resistor.

represented by a port in the simulation. The RX coil is connected to a lumped load.

IV. Equivalent Circuit and Transfer Efficiency

A. Equivalent Circuit

At SCF, the proposed AWC shown in Fig. 4 can act as a special inductor. Its input impedance is $Z_{\rm Ls} = R_{\rm Ls}(\omega) + jX_{\rm Ls}(\omega)$. The resistive part $R_{\rm Ls}(\omega)$ represents the ohmic losses and the far-field radiation loss $R_{\rm Ls}(\omega)$ remains constant except at the frequencies near the resonant points (see Fig. 5).

Fig. 12 is the equivalent circuit model of the IPT system given in Fig. 11. According to Kirchhoff's voltage law (KVL), the nodal equations for TX and RX circuits can be written, respectively, as follows:

$$I_1\left(R_s + R_{\rm Ls1}(\omega) + jX_{\rm Ls1}(\omega)\right) + j\omega M_{12} I_2 = V_s \tag{16}$$

$$I_2\left(R_{\rm load} + R_{\rm Ls2}(\omega) + jX_{\rm Ls2}(\omega)\right) + j\omega M_{12} I_1 = 0 \tag{17}$$

where $R_{\rm s}$, $R_{\rm load}$, and V_s are the source resistance, load resistance, and source voltage, respectively. At SCF, the input impedance can be written as $Z_{\rm Ls} = R_{\rm Ls} + j0$. Then (16) and (17) can be simplified as

$$I_1\left(R_{\rm s} + R_{\rm Ls1}\right) + j\omega M_{12} I_2 = V_s \tag{18}$$

$$I_2\left(R_{\rm load} + R_{\rm Ls2}\right) + j\omega M_{12} I_1 = 0. \tag{19}$$

B. Coil-to-Coil Transfer Efficiency

The output power of source, power of load, and power loss of whole IPT system can be obtained by solving (18) and (19), as follows:

$$P_{\rm out} = I_1^* \cdot V_1 = I_1^2\left(R_{\rm Ls1} + \frac{\omega^2 M_{12}^2}{R_{\rm load} + R_{\rm Ls2}}\right) \tag{20}$$

$$P_{\rm load} = I_2^* \cdot V_2 = I_1^2 \frac{\omega^2 M_{12}^2 R_{\rm load}}{\left(R_{\rm load} + R_{\rm Ls2}\right)^2} \tag{21}$$

$$P_{\rm loss} = I_1^2 R_{\rm Ls1} + I_2^2 R_{\rm Ls2} = I_1^2\left[R_{\rm Ls1} + \frac{\omega^2 M_{12}^2 R_{\rm Ls2}}{\left(R_{\rm load} + R_{\rm Ls2}\right)^2}\right]. \tag{22}$$

The transfer efficiency of two coupled AWCs (coil-to-coil efficiency) is

$$\eta_{\rm c} = \frac{P_{\rm load}}{P_{\rm out}} = \frac{\omega^2 M_{12}^2 R_{\rm load}}{R_{\rm Ls1}\left(R_{\rm load} + R_{\rm Ls2}\right)^2 + \omega^2 M_{12}^2\left(R_{\rm load} + R_{\rm Ls2}\right)}. \tag{23}$$

In a given system with known coil loss and operating frequency, the coil-to-coil transfer efficiency at a certain distance varies with the load resistance. By taking the first derivative of $\eta_{\rm c}$ with respect to $R_{\rm load}$, the maximum coil-to-coil transfer efficiency can be obtained and the best case value of $R_{\rm load}$ can be found as follows:

$$R_{\rm load} = \sqrt{\left(R_{\rm Ls1} R_{\rm Ls2} + \omega^2 M_{12}^2\right) R_{\rm Ls2} / R_{\rm Ls1}}. \tag{24}$$

C. Source-to-Load and Optimum Transfer Efficiency

The transfer efficiency of whole IPT system in Fig. 12 can be written as follows:

$$\eta_{\rm s} = \left(1 - |\Gamma|^2\right) \cdot \eta_{\rm c} \tag{25}$$

where Γ is the reflection coefficient at the input port given as $\Gamma = \frac{Z_{\rm in} - Z_{\rm s}}{Z_{\rm in} + Z_{\rm s}}$, where $Z_{\rm in} = \frac{V_1}{i_1} = R_{\rm Ls1} + \frac{\omega^2 M_{12}^2}{R_{\rm load} + R_{\rm Ls2}}$. Then, the source-to-load efficiency η_s can be expressed as

$$\eta_s = \frac{4\omega^2 M_{12}^2 R_{\rm s} R_{\rm load}}{\left[\left(R_{\rm Ls1} + R_{\rm s}\right)\left(R_{\rm load} + R_{\rm Ls2}\right) + \omega^2 M_{12}^2\right]^2}. \tag{26}$$

η_s reaches its maximum value when the output impedance of source $R_{\rm s}$ is matched to the input impedance $Z_{\rm in}$ and the load resistance $R_{\rm load}$ satisfies (24) simultaneously. Thus, the optimum transfer efficiency η_m of the IPT system can be written as (27) as shown at the bottom of this page. When both the coils are identical, i.e., $R_{\rm Ls1} = R_{\rm Ls2} = R_{\rm Ls}$, the following is obtained: (28) shown at the bottom of this page.

$$\eta_{\rm m} = \frac{\omega^2 M_{12}^2 \sqrt{\frac{\left(R_{\rm Ls1} R_{\rm Ls2} + \omega^2 M_{12}^2\right) R_{\rm Ls2}}{R_{\rm Ls1}}}}{R_{\rm Ls1}\left(\sqrt{\frac{\left(R_{\rm Ls1} R_{\rm Ls2} + \omega^2 M_{12}^2\right) R_{\rm Ls2}}{R_{\rm Ls1}}} + R_{\rm Ls2}\right)^2 + \omega^2 M_{12}^2\left(\sqrt{\frac{\left(R_{\rm Ls1} R_{\rm Ls2} + \omega^2 M_{12}^2\right) R_{\rm Ls2}}{R_{\rm Ls1}}} + R_{\rm Ls2}\right)} \tag{27}$$

$$\eta_{\rm m} = \frac{\omega^2 M_{12}^2 \sqrt{R_{\rm Ls}^2 + \omega^2 M_{12}^2}}{R_{\rm Ls}\left(\sqrt{R_{\rm Ls}^2 + \omega^2 M_{12}^2} + R_{\rm Ls}\right)^2 + \omega^2 M_{12}^2\left(\sqrt{R_{\rm Ls}^2 + \omega^2 M_{12}^2} + R_{\rm Ls}\right)} \tag{28}$$

V. Calculations of Circuit Parameters

Owing to the simple scheme of present IPT system employing AWCs, the equivalent circuit model is easier to obtain compared to the conventional magnetic coupled resonance system. Also, the transfer efficiency and other systems characteristics can be estimated directly when the coil loss $R_{\rm Ls}$ and mutual inductance M of coils are known.

A. Loss Mechanism

The loss of an AWC $R_{\rm Ls}$ is mainly caused by ohmic resistance of the coil $R_{\rm ohm}$ and the far-field radiation resistance R_r, as follows:

$$R_{\rm Ls} = R_{\rm ohm} + R_r. \tag{29}$$

On account of the proximity and the fringing effect, the ohmic loss of a coil $R_{\rm ohm}$ is larger than that of the straight wire of the same total length at the same working frequency [25]. Butterworth has done a sequence of works on ac resistances of solenoids and a series of formulae have been established [26]. In his work, the ohmic loss varies with the frequency of operation. The ratio of the wire diameter to the skin penetration depth $z = d_w/\delta$ is a key parameter, the ohmic loss $R_{\rm ohm}$ can be calculated using the appropriate equation corresponding to the value of z. Eq. (30) corresponds to the condition $z > 10$ (very high frequency) given as follows:

$$R_{\rm ohm} = R_{\rm st}\left[\alpha + \frac{1}{2}\frac{d_w^2}{s^2}\left(\beta u_1 + \gamma u_2\right)\right]. \tag{30}$$

Here, the parameters α, β, and γ are functions of wire diameter to turn spacing ratio d_w/s, u_1 and u_2 are functions of the ratio of coil length to coil diameter l/D, and $R_{\rm st}$ is the resistance of the straightened coil, which is calculated assuming a uniform current density at the surface of the wire which exponentially decays inside the conductor with the characteristic distance of the penetration depth [26]. According to (15) and the discussion in Section III-B, at SCF, the current amplitude along the wire is $|i_{x,t}| = |i_0 \sin(\omega t)\cos(\frac{2n\pi x}{l_w})|, x \in [0, l_w], n = 1, 2, 3\ldots$. Thus, the ohmic resistance of a straightened coil, considering the skin effect, can be derived by solving the power loss equation in terms of $R_{\rm st}$, as follows:

$$\int_0^{\frac{2\pi}{\omega}} i_0^2 R_{\rm st} dt = \int_0^{\frac{2\pi}{\omega}}\int_0^{l_w} \frac{|i_{x,t}|^2}{\sigma\delta\pi d_w} dx dt, \delta = \sqrt{\frac{2}{\omega\mu\sigma}} \tag{31}$$

where l_w, d_w, μ, σ, and δ are the total length, diameter, permeability, bulk conductivity, and the skin-penetration depth of the straight wire, respectively. The solution of (31) is

$$R_{\rm st} = \frac{l_w\sqrt{f\mu}}{2d_w\sqrt{\pi\sigma}}. \tag{32}$$

Meanwhile, the total radiation resistance R_r of the coil is given by the well-known formula [27]

$$R_r = 320\pi^4\left(N\frac{\pi D^2}{4\lambda^2}\right)^2. \tag{33}$$

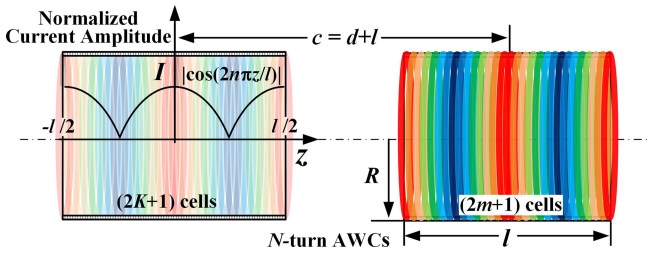

Fig. 13. Configuration of two coupled N-turn AWCs.

B. Mutual Inductance

The mutual inductance of two coupled coils has been studied widely [28]–[30]. Fig. 13 is the configuration of two coupled AWCs. The radius and length of coils are R and l, respectively.

The mutual inductance of two meshed coils carrying uniform current can be found using the filament method used in [28]. In this paper, AWCs with nonuniform current distribution are used. Thus, the filament method in [28] is modified to incorporate nonuniform current characteristics. In accordance with (15) and the discussion in Section III-B, the normalized current amplitude of AWC along the coil axis can be given as

$$|i_z'| = \left|\cos\left(\frac{2n\pi z}{l}\right)\right|,\ z \in \left[-\frac{l}{2}, \frac{l}{2}\right],\ n = 1, 2, 3\ldots \tag{34}$$

where the filament method in [28] is weighted by the normalized current amplitude to calculate the mutual inductance of two coupled coils with nonuniform current distribution. The mutual inductance M can be expressed as

$$M = \frac{N^2\sum_{g=-K}^{g=K}\sum_{s=-m}^{s=m} M'(g,s)}{\left[\sum_{g=-K}^{g=K}\left|\cos\left(\frac{2n\pi g}{2K+1}\right)\right|\right]\left[\sum_{s=-m}^{s=m}\left|\cos\left(\frac{2n\pi s}{2m+1}\right)\right|\right]}$$
$$n = 1, 2, 3\ldots \tag{35}$$

where

$$M'(g,s) = \frac{\mu_0 R}{k(g,s)}\left|\cos\left(\frac{2n\pi g}{2K+1}\right)\right|\left|\cos\left(\frac{2n\pi s}{2m+1}\right)\right| \cdot\left[\left(2-k^2(g,s)\right)K(k(g,s)) - 2E(k(g,s))\right]$$

$$k^2(g,s) = \frac{4R^2}{4R^2 + z(g,s)^2}$$

$$z(g,s) = d + l + \frac{l}{(2K+1)}g + \frac{l}{(2m+1)}s,$$

$$g = -K, \ldots, 0, \ldots K, \quad s = -m, \ldots, 0, \ldots m.$$

In above expression, $K(k)$ and $E(k)$ are complete elliptic integrals of first and second kind, respectively.

VI. Fabrication and Measurement

To validate the aforementioned analysis and the proposed IPT system, a prototype is designed, fabricated, and measured.

A. Design of Coil

The ability of a WPT system to transfer energy is determined by the factor d/D. In the following analysis, with the diameter of coil D, the conductivity σ, and diameter of wire d_w fixed, the effect of other parameters is studied.

As (14), the wire length l_w of the AWC is approximately equal to n times the wavelength λ, shown as follows:

$$l_w = N\pi D/\cos(\alpha) \approx N\pi D \approx n\lambda \,(n = 1, 2, 3\ldots) \tag{36}$$

where α is the pitch angle.

According to (35), with certain coil diameter D and transfer range d, the mutual inductance M is in direct proportion to N^2, shown as follows:

$$M \approx N^2 M_0$$

$$M_0 = \frac{\sum_{g=-K}^{g=K}\sum_{s=-m}^{s=m} M'(g,s)}{\left[\sum_{g=-K}^{g=K}\left|\cos\left(\frac{2n\pi g}{2K+1}\right)\right|\right]\left[\sum_{s=-m}^{s=m}\left|\cos\left(\frac{2n\pi s}{2m+1}\right)\right|\right]}. \tag{37}$$

For larger transfer range, the influence of coil length l to mutual induction is negligible. The average contribution of mutual induction of each turn M_0 decreases with the increase of transfer distance.

By solving (33) and (36) the radiation resistance R_r can be written as

$$R_r = n^4 \frac{20\pi^2}{N^2}. \tag{38}$$

From (32) and (36), we obtain

$$R_{\rm st} = \frac{l_w\sqrt{f\mu}}{2d_w\sqrt{\pi\sigma}} = \sqrt{\frac{l_w}{\pi}}\cdot\sqrt{l_w f}\cdot\frac{\sqrt{\mu}}{2d_w\sqrt{\sigma}}$$

$$\approx \sqrt{ND}\cdot\sqrt{nv_p}\frac{\sqrt{\mu/\sigma}}{2d_w} = \sqrt{nN}\cdot\frac{\sqrt{Dv_p\mu/\sigma}}{2d_w}$$

where $v_p = 1/\sqrt{\mu\varepsilon}$ is the light speed in wire. Thus, (39) is obtained from (30), where $R_0 = \frac{\sqrt{Dv_p\mu/\sigma}}{2d_w}[\alpha + \frac{1}{2}\frac{d_w^2}{s^2}(\beta u_1 + \gamma u_2)]$. The ohmic loss of coil $R_{\rm ohm}$ is approximately in direct proportion to $\sqrt{nN}$, shown as follows:

$$R_{\rm ohm} = R_{\rm st}\left[\alpha + \frac{1}{2}\frac{d_w^2}{s^2}(\beta u_1 + \gamma u_2)\right]$$

$$= \sqrt{nN}\cdot\frac{\sqrt{\frac{Dv_p\mu}{\sigma}}}{2d_w}\left[\alpha + \frac{1}{2}\frac{d_w^2}{s^2}(\beta u_1 + \gamma u_2)\right] = \sqrt{nN}\cdot R_0. \tag{39}$$

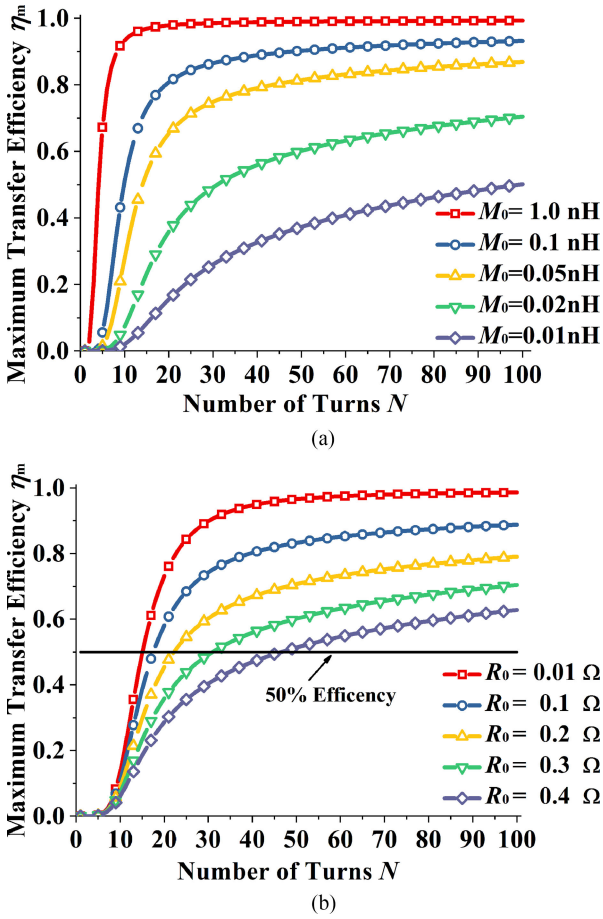

Fig. 14. Optimum transfer efficiency versus number of turns with AWCs working at the first SCF ($n = 1$). The diameter of coil D is set to be 0.07 m. (a) With R_0 set to be 0.3 Ω. (b) With M_0 set to be 0.02 nH.

Therefore, the optimum transfer efficiency can be expressed as the following equation, which is a monotonic increasing function of number of turns N: (40) shown at the bottom of this page.

Fig. 14 shows the optimum transfer efficiency $\eta_{\rm m}$ versus number of turns N when $n = 1$. It can be concluded from Fig. 14(a) that the number of turns has insignificant effect on near range power transfer. On the contrary, the more the number of turns, the higher the transfer efficiency for mid-range and far-range transfer. Fig. 14(b) reveals that with fixed transfer distance and coil diameter but with unspecified coil losses, present IPT can reach the same efficiency with proper adjustment of the number of turns. Efficiency of ~50% can be achieved by 15, 18, 23, 31, and 46 turns' coil when R_0 are 0.01, 0.1, 0.2, 0.3, and 0.4 Ω, respectively.

$$\eta_m = \frac{4c^2 {M_0}^2 n^2 N^2\sqrt{\frac{4c^2 {M_0}^2 n^2 N^2}{D^2} + \left(\frac{20n^4\pi^2}{N^2} + \sqrt{nN}R_0\right)^2}}{\left(D^2\left(\frac{20n^4\pi^2}{N^2} + \sqrt{nN}R_0 + \sqrt{\frac{4c^2 {M_0}^2 n^2 N^2}{D^2} + \left(\frac{20n^4\pi^2}{N^2} + \sqrt{nN}R_0\right)^2}\right)^2\left(\frac{20n^4\pi^2}{N^2} + \sqrt{nN}R_0 + (4c^2 {M_0}^2 n^2 N^2)/\right.\right.} \tag{40}$$
$$\left.\left.\left(D^2\left(\frac{20n^4\pi^2}{N^2} + \sqrt{nN}R_0 + \sqrt{\frac{4c^2 {M_0}^2 n^2 N^2}{D^2} + \left(\frac{20n^4\pi^2}{N^2} + \sqrt{nN}R_0\right)^2}\right)^2\right)\right)\right)$$

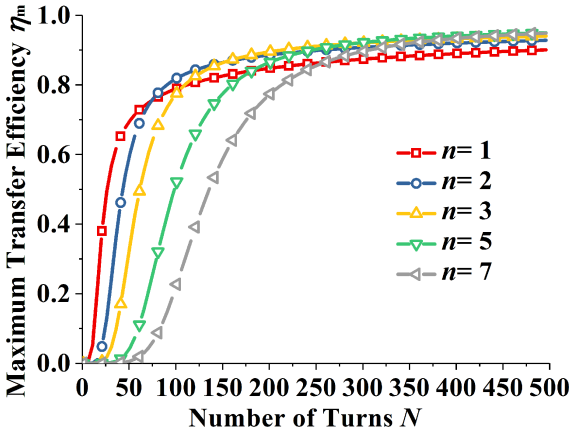

(a)

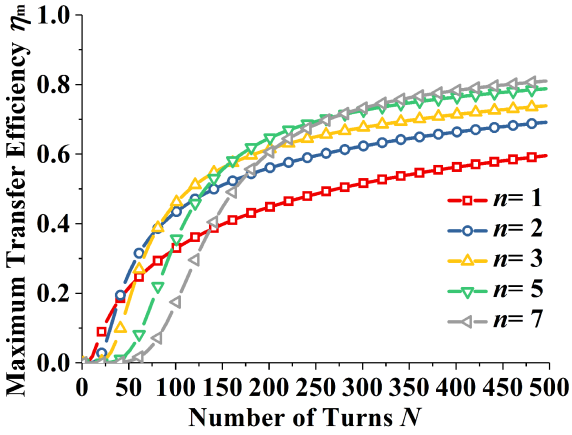

(b)

Fig. 15. Optimum transfer efficiency of AWCs of different flip numbers. The diameter of coil D is set to be 0.07 m.M_0 is set to be 0.01 nH. (a) With R_0 set to be 0.1 Ω. (b) With R_0 set to be 0.5 Ω.

The above results indicate that the IPT employing AWCs can meet the requirements for mid-range and even far-range high-efficiency energy transfer by increasing the number of turns accordingly. Additionally, the adverse effect on transfer efficiency caused by coil loss can be compensated by the positive influence of the increased number of turns. Therefore, the proposed transfer structure does not require an extremely low loss material to be used to fabricate the coils.

The effect of flip number $2n$ on transfer efficiency is divided into two conditions. As shown in Fig. 14, when the number of turns N is small, the lesser the flips number $2n$, the higher the transfer efficiency. When the number of turns N is large, the case is contrary. The primary reason for this phenomenon is that the radiation loss is sharply increased with the flips number and gradually decreased with number of turns, as expressed in (38). Moreover, the superiority of higher value of n is distinct when R_0 is large [compare Fig. 15(a) and (b)].

B. Experimental Setup

To balance the transfer performance and the processing difficulty, the number of turns is chosen to be 32. In this setup, the transfer efficiency is highest when $n = 1$.

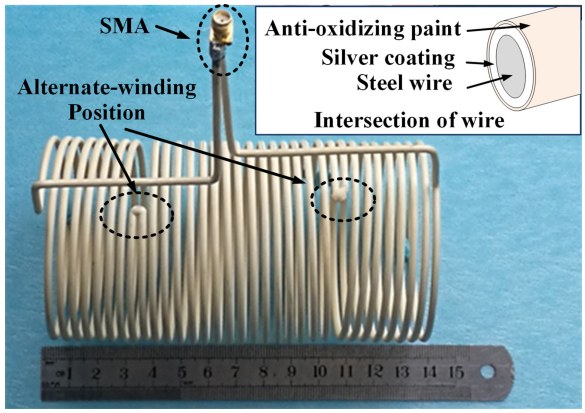

Fig. 16. Fabricated 32-turn AWC.

Fig. 16 shows the fabricated sample. To avoid deformation, the wire of coil is made of steel instead of copper. A 0.05-mm-thick silver coating and an ultrathin anti-oxidation paint is applied to the surface to reduce the ohmic loss. In this design, the skin depth $\sqrt{2/\omega\mu\sigma} \approx 0.007$ mm is far less than the total thickness of silver coating. The diameter D, length l, wire diameter d_w, and total length of wire l_w are 70, 140, 2.6 (including silver coating), and 7177 mm, respectively. The average distance s between centers of two adjacent loops is 4.375 mm.

Using (36), (30), and (33), the SCF f, ohmic loss $R_{\rm ohm}$, and radiation resistance R_r are found to be 41.8 MHz, 1.54, and 0.19 Ω, respectively. The total loss $R_{\rm Ls}$ of a single AWC can be measured by vector network analyzer (VNA) when removing another coil. The measured resistance of these two AWCs are both about 1.9 ± 0.2 ohms, which meets well with the calculated value (1.73 Ω). The minor difference may be caused by the nonuniform turn spacing and soldering inaccuracies of the SubMiniature version A (SMA) connector. The mutual inductance M_{12} is calculated by taking $K = m = 20$ under various transfer distance, shown in Table I. In addition, the optimum transfer range and the corresponding load/input impedance are calculated using (23) and (26), respectively. Identical load and input impedance are resulted when $R_{\rm Ls1} = R_{\rm Ls2}$. In this setup, nearly half of the total energy can be transferred to a distance of 420 mm, i.e., 6 times the coil diameter, as seen from Table I.

C. Measurement of Transfer Efficiency

The source-to-load transfer efficiency η_s can be measured using VNA. Later, the coil-to-coil transfer efficiency η_c can be calculated using (25).The experimental configuration is shown in Fig. 17. The TX and RX coils are connected to ports 1 and 2 of VNA via coaxial lines. The two coils are aligned coaxially, the distance between them is d.

From Table I, to realize the optimum transfer efficiency at the distance of six times the coil diameter, load and source resistances of 5.1 Ω are needed. This resistance can be realized by using a pair of quarter-wavelength 16-Ω transmission lines between coil and VNA. In practice, three 50-Ω coaxial lines can be connected in parallel to realize such transmission lines. To make a comparison, the transfer efficiency η_s and

TABLE I
CALCULATED MUTUAL INDUCTANCE AND OPTIMUM TRANSFER EFFICIENCY

Transfer distance d(mm)	d/D	Mutual inductance* M_{12}(nH)	Input impedance $Z_{\text{in}}(\Omega)$	Load impedance $R_{\text{load}}(\Omega)$	Optimum transfer efficiency η_{m}
35	0.5	1145.3	300.07	300.07	98.9%
70	1.0	523.52	137.17	137.17	97.5%
105	1.5	287.74	75.41	75.41	95.5%
140	2.0	177.17	46.45	46.45	92.8%
175	2.5	117.69	30.88	30.88	89.4%
210	3.0	82.53	21.69	21.69	85.2%
245	3.5	60.29	15.89	15.89	80.4%
280	4.0	45.48	12.04	12.04	74.9%
315	4.5	35.20	9.38	9.38	68.9%
350	5.0	27.83	7.49	7.49	62.5%
385	5.5	22.40	6.12	6.12	55.9%
420	6.0	18.31	5.10	5.10	49.3%
455	6.5	15.16	4.33	4.33	42.9%
490	7.0	12.70	3.75	3.75	36.9%
525	7.5	10.75	3.31	3.31	31.3%
560	8.0	9.18	2.96	2.96	26.3%
595	8.5	7.90	2.70	2.70	21.9%
630	9.0	6.85	2.50	2.50	18.1%
665	9.5	5.98	2.34	2.34	14.9%
700	10.0	5.25	2.21	2.21	12.2%
735	10.5	4.61	2.11	2.11	10.1%
770	11.0	4.11	2.04	2.04	8.2%
805	11.5	3.68	1.98	1.98	6.7%
840	12.0	3.28	1.93	1.93	5.5%

The values of input impedance and load impedance in the table are calculated by (12) and (15) for achieving optimum transfer efficiency.
$*$ Mutual inductance M_{12} is calculated under $K = m = 20$.

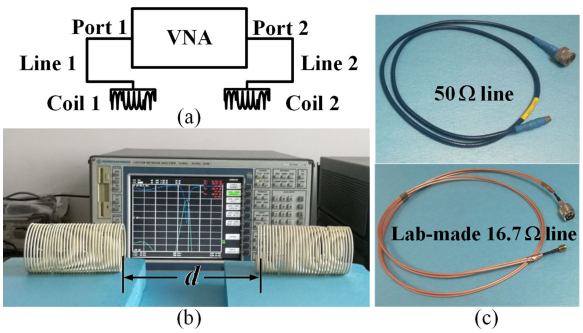

Fig. 17. Diagrams of the experimental setup. The TX and RX coils are connected to port 1 and port 2 of VNA. (a) Sketch of experiment setup. (b) Photograph of the experiment setup. The transfer distance is 210 mm in this figure. (c) Coaxial lines used in experiments.

η_c when $R_{\text{s}} = R_{\text{load}} = 50\ \Omega$ are also measured by using 50-Ω coaxial line.

Comparisons of theoretical and experimental results of AWCs are given in Fig. 18(a) and (b). It can be seen that there is good agreement between measured data and theoretical predictions. About 50% power transfer efficiency is obtained for a transfer range, i.e., 6 times the coil diameter. Further, the measured transfer efficiencies of conventional coils with same geometry (same turn number, same coil diameter, same coil length, and same coil pitch) fabricated by the same wire at its own SCF are also included in Fig. 18(a) and (b). The comparison of the theoretical maximum transfer efficiency of AWCs, traditional coils with same size at optimum frequency, and at their own SCF is given in Fig 18(c). It is prominent that AWCs performance exceeds the performance of a conventional coil significantly.

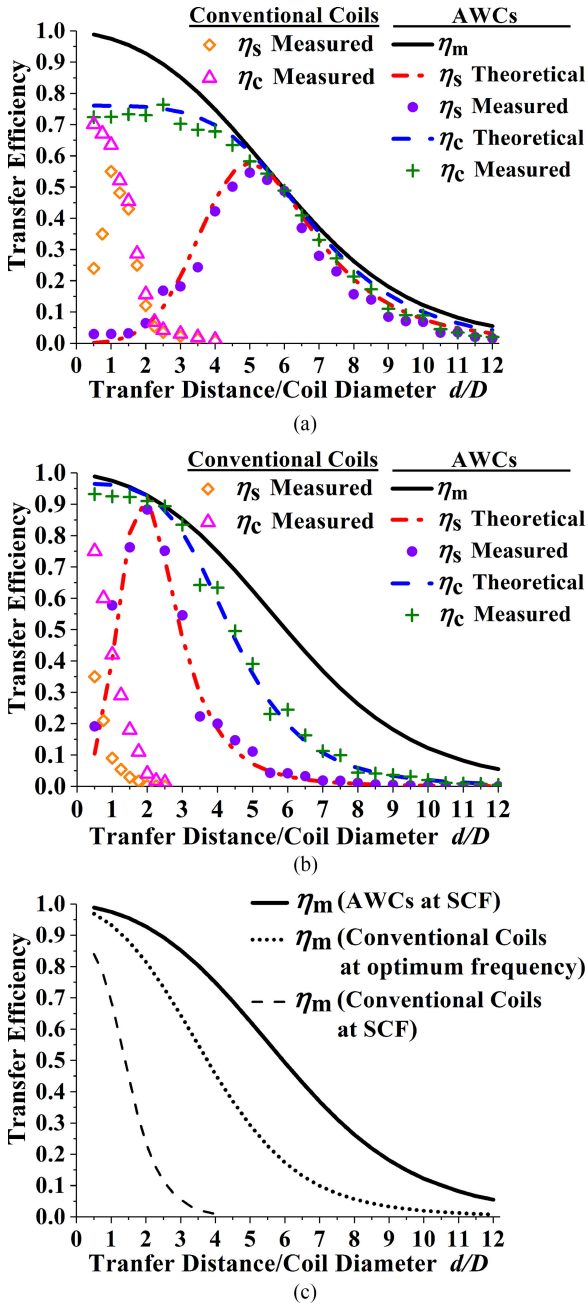

Fig. 18. Experimental results compared with the theoretical predictions. (a) With a lab-made 1.2-m-long 16.7-ohms coaxial line (1/4 wavelength) and (b) With a 50-ohms coaxial line. (c) Comparison of maximum transfer efficiency among conventional coils and AWCs with same geometry.

A transfer experiment with an electrical appliance is carried out. The experimental setup and the full view of experiment are as shown in Fig. 19(a) and (b), respectively. The small signal produced by a signal generator is amplified by the RF amplifier supplied with a dc source, and then fed to the TX coil through a 16.7 Ω coaxial line with $\lambda/4$ length. The RX coil is directly connected to the bulb using SMA adaptors and a bulb holder, as seen in Fig. 19(c). The resistance of bulb is measured in glowing state as 5.4 Ω (label "1.5 V, 0.3 A"). The distance between TX and RX coils is 420 mm (6 times the coil diameter). The power

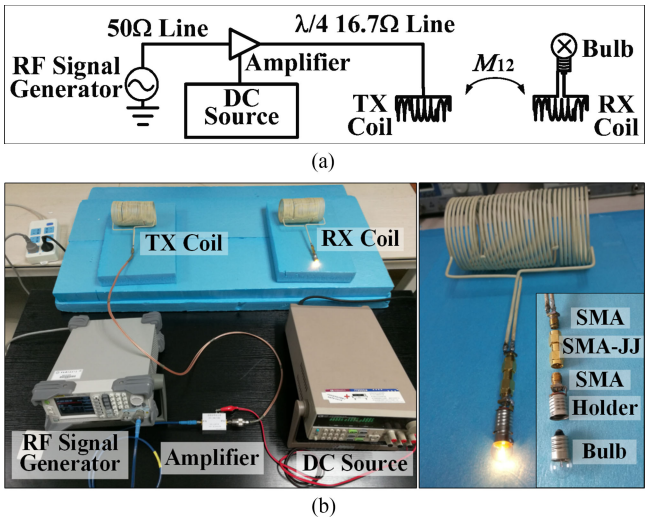

Fig. 19. Inductive power transfer experiment with power up to a useful level. (a) Sketch of transfer setups. (b) Full view of experiment. (c) Details of the connection structure between RX coil and bulb.

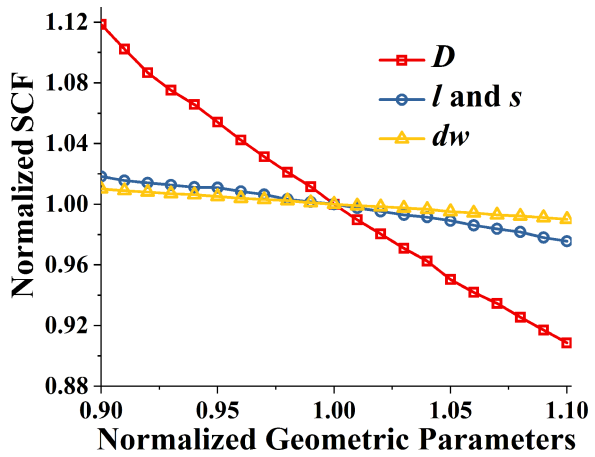

Fig. 20. Simulated result of normalized SCF versus normalized geometric parameters. The initial value of parameters is the same as previous part.

level of signal generator is set to be −10 dBm and amplifier gain is 39.08 dB at this input power level.

D. Sensitivity of Operating Frequency

The SCF of AWC coil is related to its geometry and simulation is carried out to study the relationship between them. In the simulation, the initial value of the geometry parameters D, l, s, and $d_{\rm w}$ are the same as the previous part and other parameters are kept constant when sweeping any one of them. Simulation results shown in Fig. 20 demonstrate the normalized SCF versus the variation of geometry parameters, where l and s are coupled as $l = Ns$. The SCF is not sensitive to l, s, and

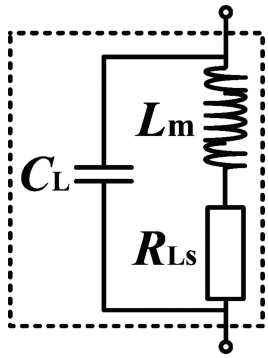

Fig. 21. Refined equivalent circuit of alternate-winding coil.

d_w and is approximately inversely proportional to D which can be explicated by $l_w \approx N\pi D \approx \lambda = c/f$, as shown in (36). In the actual manufacturing process, the precision of D can be controlled under 0.14% by controlling the total length of the coil wire l_w, i.e., 10 mm deviation over 7177 mm. Considering the information provided in Fig. 20, the frequency difference between the two AWCs is less than 0.06 MHz.

An equivalent circuit including a parallel capacitor [31] is employed to investigate the effect of capacitance between different turns, as shown in Fig. 21. The analytical expression of parasitic capacitance of N-turn round wire solenoidal coil with an insulation coating can be derived as [31] equation (41) shown at the bottom of this page, where t and ε_r are the thickness and relative permittivity of the insulation coating, respectively.

By using Taylor series expansion, at the frequencies close to SCF ω_0, the impedance of the main inductor $L_{\rm m}$ can be expressed as

$$\begin{aligned} jX(\omega) &= j\left[X(\omega_0) + (\omega-\omega_0)X'(\omega_0) + O\left[(\omega-\omega_0)\right]\right] \\ &\approx j(\omega-\omega_0)k_L \end{aligned} \tag{42}$$

where $k_L = X'(\omega_0)$ is the slope of the imaginary curve at the SCF.

Thus, the input impedance of the AWC can be written as

$$\begin{aligned} Z_{\rm total} &= \frac{1}{\frac{1}{jX(\omega)+R_{\rm Ls}} + j\omega C_{\rm L}} = \frac{1}{\frac{1}{j(\omega-\omega_0)k_L+R_{\rm Ls}} + j\omega C_{\rm L}} \\ &= \frac{R_{\rm Ls} + j\left[(\omega-\omega_0)k_L - \omega C_{\rm L}(\omega-\omega_0)^2 {k_L}^2 - {R_{\rm Ls}}^2\omega C_{\rm L}\right]}{\left(1-\omega C_{\rm L}(\omega-\omega_0)k_L\right)^2 + \left(R_{\rm Ls}\omega C_{\rm L}\right)^2}. \end{aligned} \tag{43}$$

When the imaginary part of $Z_{\rm total}$ is set to be zero, the frequency shift can be deduced to

$$\Delta f = (\omega-\omega_0)/2\pi = \frac{1-\sqrt{1-4{C_{\rm L}}^2{R_{\rm Ls}}^2\omega^2}}{4\pi C_{\rm L}k_L\omega} \tag{44}$$

$$C_L = \begin{cases} \dfrac{\pi^2 D\varepsilon_0}{(N-1)\ln\left(s/d_w + \sqrt{(s/d_w)^2-1}\right)} & (t \ll s-d_w) \\ \dfrac{\pi^2 D\varepsilon_0}{(N-1)\ln\left(P+\sqrt{P^2-(1+2t/d_w)^{2/\varepsilon_r}}\right)}, \quad P = \dfrac{s}{d_w(1+2t/d_w)^{1-1/\varepsilon_r}} & (t \sim s-d_w) \end{cases} \tag{41}$$

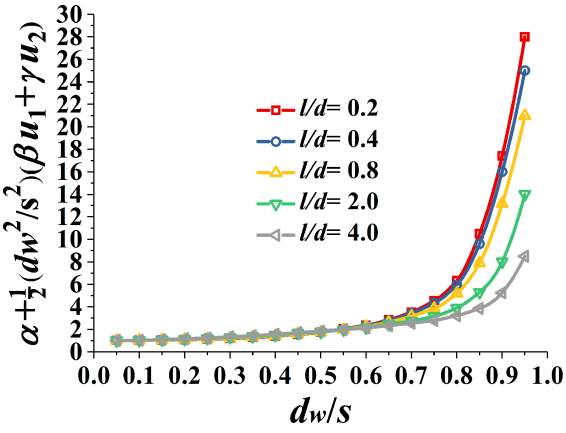

Fig. 22. Factor F versus the ratio of wire diameter to adjacent turn distance d_w/s for different l/d.

where the other root $\frac{1+\sqrt{1-4{C_{\rm L}}^2{R_{\rm Ls}}^2\omega^2}}{4\pi C_{\rm L}k_L\omega}$ is removed because it is not close to SCF.

The numerical calculation of (44) reveals that the frequency shift caused by parasitic capacitance between turns of coil is negligible.

E. Sensitivity of Transfer Efficiency

The sensitivity analysis of transfer efficiency is carried out and the main factors are listed below as three subsections.

1) Ratio of Pitch to Wire Diameter: It is observed that the transfer efficiency is sensitive to the pitch s and wire diameter d_w if the ratio $d_w/s > 0.7$. It can be seen from (28) that the transfer efficiency is affected by operating frequency ω, mutual inductance M, radiation loss R_r, and the ohmic loss of coil $R_{\rm ohm}$. It can be easily deduced that the first three factors are not sensitive to coil geometry. According to (30), $R_{\rm ohm}$ is the product of $R_{\rm st}$ and the factor $F = [\alpha + \frac{1}{2}\frac{d_w^2}{s^2}(\beta u_1 + \gamma u_2)]$ which represents the contribution of the proximity effect and the fringing effect. Obviously, $R_{\rm st}$ is not sensitive to the coil geometry according to (31). Thus, the performance of factor F is important and needs to be discussed. The numerical values of factor F are calculated based on [26] and shown in Fig. 22. A quick glance at Fig. 22 suggests that the ohmic loss of coil increases sharply when $d_w/s > 0.7$. To avoid the declination in transfer efficiency, an optimal range of $d_w/s < 0.7$ is suggested in design stage.

2) SCF Disparity between TX and RX Coils: The transfer efficiency will diverge from (27) if the SCFs of TX and RX coils are not identical, where the difference of the SCFs is further defined by geometry deviations in manufacturing stage, as seen in Fig. 20.

Assuming that the SCFs of the TX and RX coils are ω_T and ω_R, respectively, in this case, the nodal equations (KVL) of these two coils around the center operating frequency $\omega_c = (\omega_T + \omega_R)/2$ can be obtained as follows by putting (42) in to (16) and (17):

$$I_1\left(R_s + R_{Ls1} + jk_{\rm L1}\left(\omega_T - \omega_c\right)\right) + j\omega M_{12}I_2 = V_s \quad (45)$$

$$I_2\left(R_{\rm load} + R_{Ls2} + jk_{\rm L2}\left(\omega_R - \omega_c\right)\right) + j\omega M_{12}I_1 = 0. \quad (46)$$

Then the active output power and power consumed by load can be deduced as

$$P_{\rm act} = I_1^* \cdot V_1 = I_1^2\left(R_{\rm Ls1} + \frac{\omega_c^2 M_{12}^2\left(R_{\rm load} + R_{\rm Ls2}\right)}{\left(R_{\rm load} + R_{\rm Ls2}\right)^2 + k_{\rm L2}^2(\omega_R - \omega_c)^2}\right) \quad (47)$$

$$P_{\rm load} = I_2^* \cdot V_2 = I_1^2\frac{\omega_c^2 M_{12}^2 R_{\rm load}}{\left(R_{\rm load} + R_{\rm Ls2}\right)^2 + k_{\rm L2}^2(\omega_R - \omega_c)^2}. \quad (48)$$

The transfer efficiency of two coupled AWCs is equation (49) shown at the bottom of this page.

The input impedance can be expressed as

$$Z_{\rm in} = \frac{V_1}{i_1} = R_{\rm Ls1} + jk_{\rm L1}\left(\omega_T - \omega_c\right) + \frac{\omega_c^2 M_{12}^2}{R_{\rm load} + R_{\rm Ls2} + jk_{\rm L2}\left(\omega_R - \omega_c\right)}. \quad (50)$$

According to (25) and (50), the source-to-load efficiency $\eta_{\rm s}$ can be expressed as (51), shown at the bottom of this page.

For two similar AWCs, $R_{\rm Ls1} \approx R_{\rm Ls2} \approx R_{\rm Ls}$, $k_{\rm L1} \approx k_{\rm L2} \approx k_{\rm L}$, (51) can be deduced as

$$\eta_s = \frac{4M^2 R_{\rm load}R_s\omega_c^2\left(\left(R_{\rm Ls} + R_{\rm load}\right)^2 + {k_L}^2(\Delta\omega/2)^2\right)}{\begin{array}{c}\left(M^2(R_{\rm Ls} + R_{\rm load})\omega_c^2 + (R_{\rm Ls} + R_s)\right.\\ \left.\left(\left(R_{\rm Ls} + R_{\rm load}\right)^2 + {k_L}^2(\Delta\omega/2)^2\right)\right)^2\\ + \left(k_L(\Delta\omega/2)\left(\left(R_{\rm Ls} + R_{\rm load}\right)^2 + {k_L}^2(\Delta\omega/2)^2\right)\right.\\ \left. - k_{\rm L}M^2\omega_c^2(\Delta\omega/2)\right)^2\end{array} \quad (52)$$

where $\Delta\omega = \omega_T - \omega_R$.

$$\eta_c = \frac{P_{\rm load}}{P_{\rm act}} = \frac{\omega_c^2 M_{12}^2 R_{\rm load}}{R_{\rm Ls1}\left(\left(R_{\rm load} + R_{\rm Ls2}\right)^2 + k_{\rm L2}^2(\omega_R - \omega_c)^2\right) + \omega_c^2 M_{12}^2\left(R_{\rm load} + R_{\rm Ls2}\right)} \quad (49)$$

$$\eta_s = \frac{4M^2 R_{\rm load}R_{\rm s}\omega_c^2\left(\left(R_{\rm Ls2} + R_{\rm load}\right)^2 + {k_{\rm L2}}^2(\omega_R - \omega_{\rm c})^2\right)}{\begin{array}{c}\left(M^2\left(R_{\rm Ls2} + R_{\rm load}\right)\omega_c^2 + \left(R_{\rm Ls1} + R_{\rm s}\right)\left(\left(R_{\rm Ls2} + R_{\rm load}\right)^2 + {k_{\rm L2}}^2(\omega_R - \omega_{\rm c})^2\right)\right)^2\\ + \left(k_{\rm L1}\left(\omega_T - \omega_{\rm c}\right)\left(\left(R_{\rm Ls2} + R_{\rm load}\right)^2 + {k_{\rm L2}}^2(\omega_R - \omega_{\rm c})^2\right) - k_{\rm L2}M^2\omega_c^2\left(\omega_R - \omega_{\rm c}\right)\right)^2\end{array} \quad (51)$$

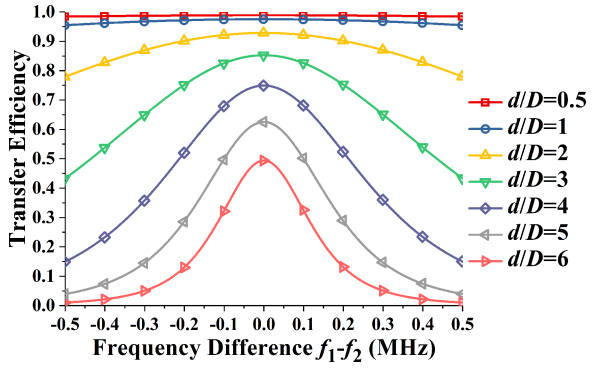

Fig. 23. Transfer efficiency versus frequency difference. The parameters of AWC are the same as the coil used in previous parts.

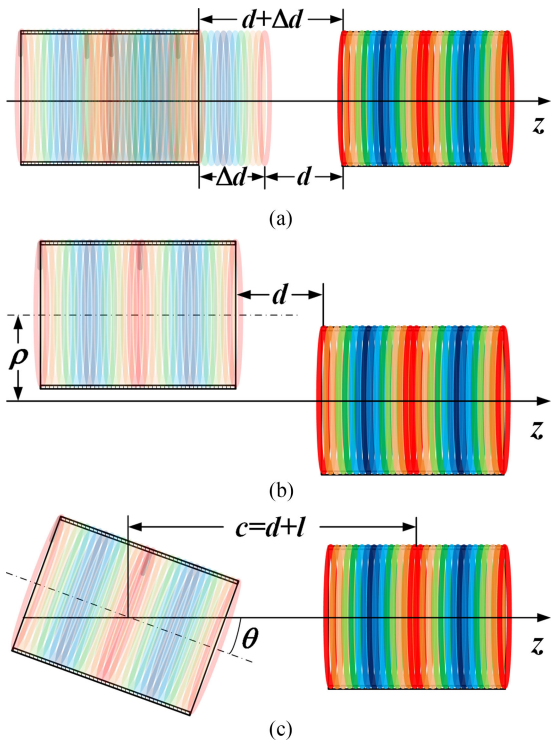

Fig. 24. Sketches of (a) axial, (b) lateral, and (c) angular misalignments.

Fig. 23 shows the calculated transfer efficiency versus frequency difference at different distances. In the calculation, $\mathrm{R_{Ls}}$ is 1.73 Ω (as calculated in Section VI) and k_L is 1.29×10^{-5} (determined by simulation). Moreover, M, R_{load}, and R_{s} are given in Table I. It can be seen that the transfer efficiency is not sensitive to frequency difference (related to geometry deviations) when the coupling between two coils is strong.

3) Axial, Lateral, and Angular Misalignments: In practical scenarios, the transfer efficiency will reduce if the transfer coils are axially, laterally, or angularly misaligned. For a well-designed IPT system, the misalignments change the mutual inductance M_{12} and cause the system mismatch. The system transfer efficiency η_{s} is used here to study the sensitivity instead of the maximum efficiency η_{m}, because the later one does not take into account the power reflected from the source and load. When misalignments occur, the parameters including ω, R_{s}, R_{load}, R_{Ls1}, and R_{Ls2} will not change. Therefore, in the analysis and calculation below, these parameters are kept constant.

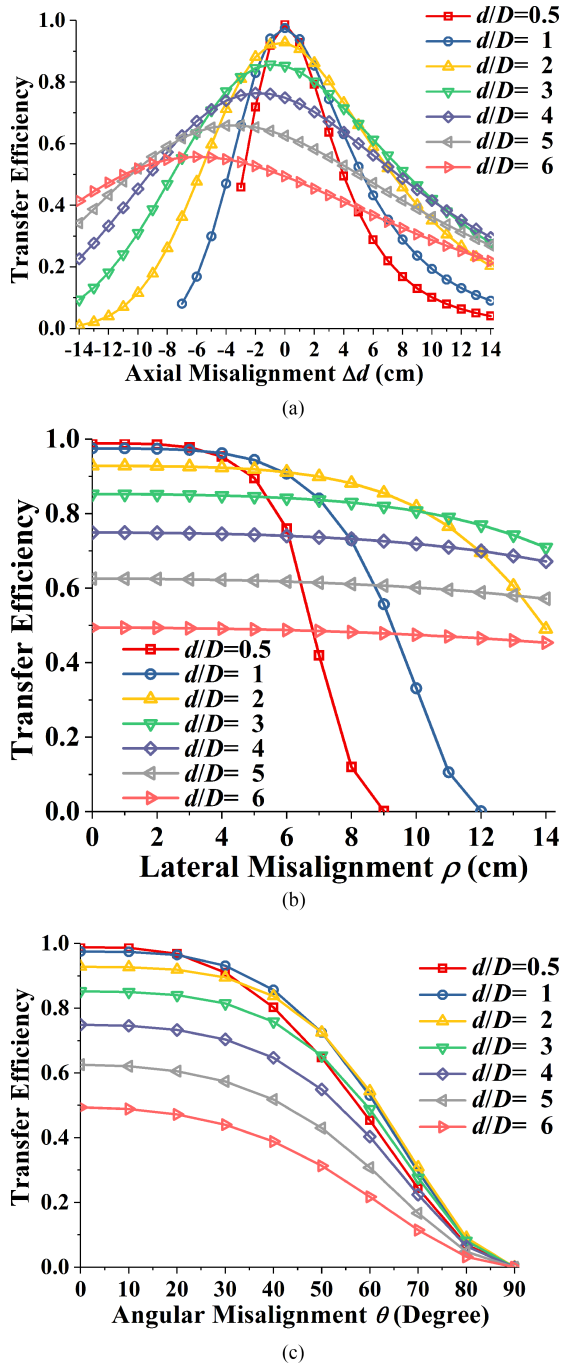

Fig. 25. Transfer efficiency versus misalignment. (a) Axially misaligned. (b) Laterally misaligned. (c) Angularly misaligned.

In the calculation, the mutual inductance of misaligned coils can be calculated through a similar process, as shown in Section V-B, consulting the formulas given in [32] and [33]. The sensitivity reports of efficiency versus axial, lateral, and angular misalignments are shown in Fig. 25(a)–(c), respectively.

Looking at Fig. 25, the conclusion can be depicted that system efficiency tends to be more sensitive to axial misalignment for shorter transfer distances. Longer transfer distances are relatively less sensitive to axial misalignment. Same is the case with

TABLE II
PARAMETERS OF AWCs OPERATING AT 13.56 MHz

Turn number N	Coil diameter D(m)	Coil length l(m)	Coil loss $R_{\rm Ls}(\Omega)$	Aspect ratio l/D
4	0.896	0.017	2.35	0.02
8	0.454	0.035	1.72	0.08
12	0.331	0.052	1.78	0.16
16	0.274	0.069	1.90	0.25
20	0.236	0.087	2.04	0.37
24	0.206	0.104	2.10	0.50
28	0.190	0.121	2.24	0.64
32	0.177	0.139	2.35	0.79
36	0.166	0.156	2.45	0.94
40	0.158	0.173	2.58	1.09
...	...	...	...	...

The geometry parameters of AWCs are calculated by (25) when letting $n = 1$ and then amended by simulations. Coil loss is obtained from (18) to (22).

lateral misalignment. This phenomenon can be explained as the relative change of distance is large when the coils are close to each other. On the other hand, transfer efficiency is not much sensitive to angular misalignment for either longer or shorter transfer distances.

VII. DESIGN EXAMPLE OF IPT SYSTEM EMPLOYING ACWs

A. *Design Example for Given Operating Frequency*

In Section VI, an IPT system employing a pair of ACWs with fixed coil diameters is presented. In this section, this IPT system is designed to operate at 13.56 MHz (one of the industrial, scientific and medical (ISM) bands) to meet the practical design task.

Table II shows the design paramters of the coil with different geometries and sizes. The coils with more turns would have smaller coil diameter and longer coil length as seen from Table II. When the operating frequency of IPT system is given (13.56 MHz in this case), the geometric dimensions of coils can be decided depending on the application requirements. In this design, the coil wire is the same as that of in Section VI and d_w/s is set to be 0.6. Keeping the pitch s uniform and wire diameter d_w fixed, different turn number N will result in different coil length $l = N \times s$. The only variable parameter in this case is the coil diameter D, which can be adjusted to achieve the desired frequency. A smaller D for same coil length l and number of turns N would result in smaller wire length and higher operating frequency and vise versa. Here, operating frequency is chosen to be 13.56 MHz, thus the corresponding coil diameter D is deduced accordingly. Finally, the $R_{\rm Ls}$ is calculated by using (18)–(22).

Besides, the maximum transfer efficiency of these AWCs versus transfer distance have been calculated and shown in Fig. 26 through the same process as in Section VI. It can be concluded that less number of turns result in longer transfer distance but the normalized transfer distance is reduced when the number of turns is small and vice versa for more number of turns.

In the current demonstration, a pair of 16-turn AWCs prototype is fabricated and tested as an example. The measured individual resistance of these two AWCs at SCF are $2.1 \pm 0.2\ \Omega$. The measured transfer efficiencies between these two AWCs when connected directly to 50-Ω line are shown in Fig. 27. About 90% power transfer efficiency is achieved with $d = 0.55$ m and more than 50% system transfer efficiency can be obtained for a transfer distance ranging 0.4 m $< d <$ 0.75 m. This proves that the IPT system can obtain good performance when directly connected to the commercial RF power stage without any matching networks.

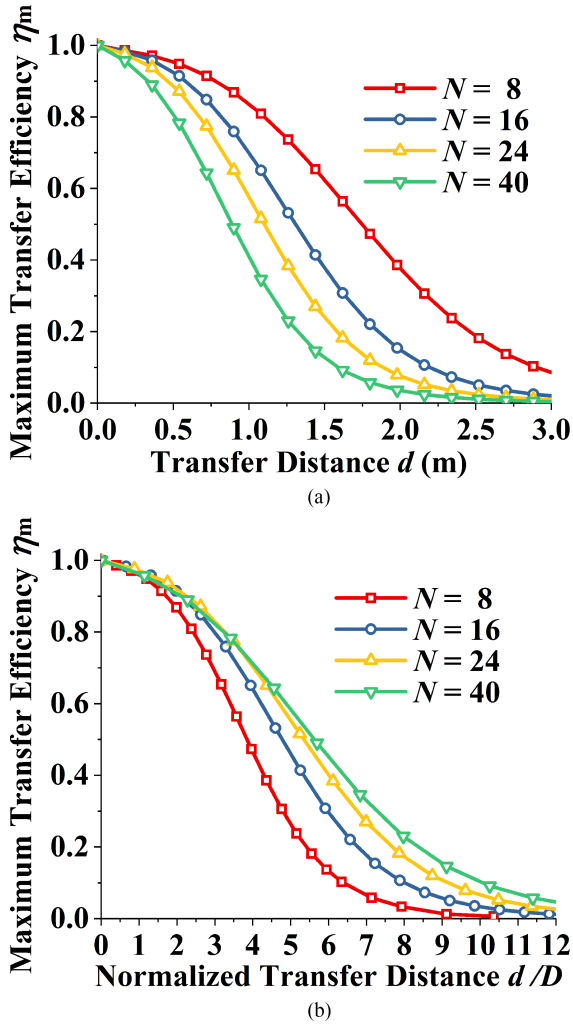

Fig. 26. Optimum transfer efficiency of AWCs with different turn numbers (a) versus transfer distance and (b) versus normalized transfer distance.

An experiment is carried out to validate the viability of the IPT system employing AWCs in practical applications, as shown in Fig. 28. In this experiment, the designed IPT system is used to drive a LED monitor (13-W dc appliance) without surplus matching networks. A two-stage power amplifier is connected to the RF generator, with the output power of primary and secondary stages set to be 1 and 17.5 W, respectively. The LED monitor, a voltage regulator, and a bridge rectifier are connected in series to employ as the load for the RX coil. The transfer distance d is set to be 0.55 m. Measured by an oscilloscope, the input power of TX coil, output power of RX coil, and receiving power of LED monitor are 17.46, 15.93, and 13.11 W, respectively. It indicates that the measured transfer efficiency between

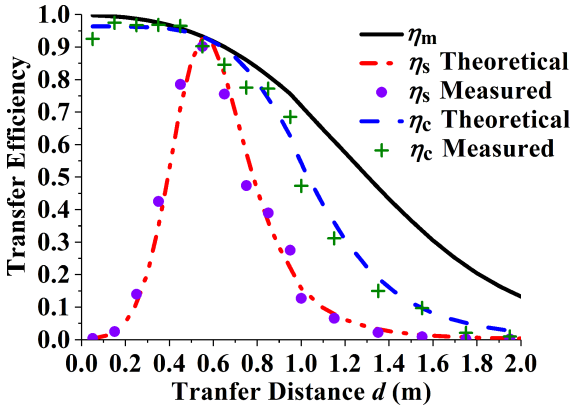

Fig. 27. Experimental transfer efficiencies of 16-turn AWCs compared with the theoretical predictions. The AWCs are connected to VNA with 50-ohms coaxial line.

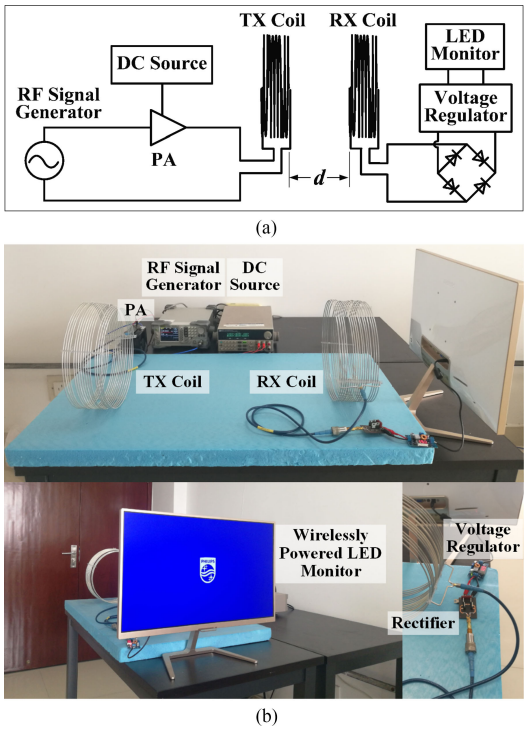

Fig. 28. Practical transfer demonstration at commercial power level. (a) Experiment settings. (b) Wirelessly powered LED monitor.

TX and RX coils reaches about 91%. While from power amplifier (PA) to the LED monitor, about 75% transfer efficiency is achieved by the system without any matching networks.

B. Tradeoff of the Coil Size and the SCF

It can be seen from Table II that the SCF is closely related to AWC's diameter and its number of turns. The tradeoff is shown below in Fig. 29. The SCF of AWCs with variable coil diameters and different number of turns are obtained by employing the finite element modeling simulation software, as shown in Fig. 29. In this figure, the range of coil diameters are from 0.05 to 1 m, and the number of turns are between 4 and 52. The available range of SCF by employing the AWCs with these parameters is 2–300 MHz. Meanwhile, the effect of coil length to SCF is

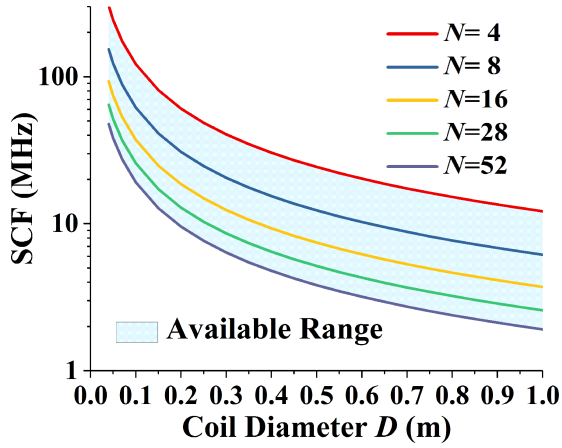

Fig. 29. SCF as a function of coil size and number of turns. The available range of SCF is highlighted by pale blue.

negligible. The coil length is approximately equal to the product of the number of turns N and the distance s between the centers of two adjacent loops. The coils with same turns N and diameter D but different distances s have almost the same SCF, the same is also observed in simulations. This phenomenon is interpreted in Section VI-D.

VIII. Conclusion

A novel coil for high-efficiency mid-range IPT is proposed and analyzed. The equivalent circuit of IPT with a pair of AWCs is established. The analytical expressions for coil-to-coil, source-to-load, and optimum transfer efficiency are calculated mathematically. The proposed IPT system does not require surplus compensation network for input/output impedance matching, avoiding the complex and tedious design of compensating networks that in fact are essential for traditional IPT systems. Further, it has been justified that it is not always mandatory to use low-loss coil material because the coil losses can be compensated by increasing the number of turns; this makes the system more application oriented. Experimental observations reveal that the proposed IPT configuration can achieve a transfer range up to 6 times the coil diameter with the power transfer efficiency of ∼50%, reduced complexity, and practical feasibility that have previously been unrealizable. A 13.56-MHz IPT system employing a pair of AWCs without any matching networks is designed, fabricated, and tested. Meanwhile, the sensitivities of the proposed AWCs and IPT system are studied. To validate the feasibility of the system at a useful power level, a LED monitor is driven wirelessly as a demonstration. Nevertheless, depending on the design requirements, an IPT system using the proposed method can be designed to have better transfer performance.

References

[1] A. Sahai and D. Graham, "Optical wireless power transmission at long wavelengths," in *Proc. Int. Space Opt. Syst. Appl. Conf.*, May 2011, pp. 164–170.
[2] K. Huang and V. K. N. Lau, "Enabling wireless power transfer in cellular networks: Architecture, modeling and deployment," *IEEE Trans. Wireless Commun.*, vol. 13, no. 2, pp. 902–912, Feb. 2014.
[3] G. A. Landis, "Charging of devices by microwave power beaming," U.S. Patent 6 967 462, Nov. 22, 2005.

[4] A. Kurs, A. Karalis, R. Moffatt, J. D. Joannopoulos, P. Fisher, and M. Soljacic, "Wireless power transfer via strongly coupled magnetic resonances," *Science*, vol. 317, no. 5834, pp. 83–86, Jul. 2007.
[5] A. Karalis, J. Joannopoulos, and M. Soljacic, "Efficient wireless non-radiative mid-range energy transfer," *Ann. Phys.*, vol. 323, no. 1, pp. 34–48, Jan. 2008.
[6] T. Imura and Y. Hori, "Maximizing air gap and efficiency of magnetic resonant coupling for wireless power transfer using equivalent circuit and Neumann formula," *IEEE Trans. Ind. Electron.*, vol. 58, no. 10, pp. 4746–4752, Oct. 2011.
[7] A. P. Sample, D. A. Meyer, and J. R. Smith, "Analysis, experimental results, and range adaptation of magnetically coupled resonators for wireless power transfer," *IEEE Trans. Ind. Electron.*, vol. 58, no. 2, pp. 544–554, Feb. 2011.
[8] F. Musavi and W. Eberle, "Overview of wireless power transfer technologies for electric vehicle battery charging," *IET Power Electron*., vol. 7, no. 1, pp. 60–66, Jan. 2014.
[9] N. Shinohara, "Power without wires," *IEEE Microw. Mag.*, vol. 12, no. 7, pp. S64–S73, Dec. 2011.
[10] S. Kim, G. Covic, and J. Boys, "Tripolar pad for inductive power transfer systems for ev charging," *IEEE Trans. Power Electron.*, vol. 32, no. 7, pp. 5045–5057, Jul. 2017.
[11] M. Budhia, G. Covic, and J. Boys, "Design and optimization of circular magnetic structures for lumped inductive power transfer systems," *IEEE Trans. Power Electron.*, vol. 26, no. 11, pp. 3096–3108, Nov. 2011.
[12] B. Cannon, J. Hoburg, D. Stancil, and S. Goldstein, "Magnetic resonant coupling as a potential means for wireless power transfer to multiple small receivers," *IEEE Trans. Power Electron.*, vol. 24, no. 7, pp. 1819–1825, Jul. 2009.
[13] B. Lenaerts and R. Puers, "An inductive power link for a wireless endoscope," *Biosens. Bioelectron.*, vol. 22, no. 7, pp. 1390–1395, 2007.
[14] S. Tianjia, X. Xiang, L. Guolin, G. Yingke, D. Yangdong, and W. Zhihua, "A two-hop wireless power transfer system with an efficiency-enhanced power receiver for motion-free capsule endoscopy inspection," *IEEE Trans. Biomed. Eng.*, vol. 59, no. 11, pp. 3247–3254, Nov. 2012.
[15] M. R. Basar, M. Y. Ahmad, J. Cho, and F. Ibrahim, "Application of wireless power transmission systems in wireless capsule endoscopy: An overview," *Sensors*, vol. 14, no. 6, pp. 10929–10951, Jun. 2014.
[16] M. J. Chabalko and A. P. Sample, "Three-dimensional charging via multimode resonant cavity enabled wireless power transfer," *IEEE Trans. Power Electron.*, vol. 30, no. 11, pp. 6163–6173, Nov. 2015.
[17] J. Shin *et al.*, "Design and implementation of shaped magnetic-resonance-based wireless power transfer system for roadway-powered moving electric vehicles," *IEEE Trans. Ind. Electron.*, vol. 61, no. 3, pp. 1179–1192, Mar. 2014.
[18] S. Y. R. Hui, W. X. Zhong, and C. K. Lee, "A critical review of recent progress in mid-range wireless power transfer," *IEEE Trans. Power Electron.*, vol. 29, no. 9, pp. 4500–4511, Sep. 2014.
[19] Z. N. Low, R. A. Chinga, R. Tseng, and J. Lin, "Design and test of a high-power high-efficiency loosely coupled planar wireless power transfer system," *IEEE Trans. Ind. Electron.*, vol. 56, no. 5, pp. 1801–1812, May 2009.
[20] G. A. Covic and J. T. Boys, "Inductive power transfer," *Proc. IEEE*, vol. 101, no. 6, pp. 1276–1289, Jun. 2013.
[21] W. Zhang, S. C. Wong, C. K. Tse, and Q. Chen, "Analysis and comparison of secondary series- and parallel-compensated inductive power transfer systems operating for optimal efficiency and load-independent voltage-transfer ratio," *IEEE Trans. Power Electron.*, vol. 29, no. 6, pp. 2979–2990, Jun. 2014.
[22] M. Pinuela, D. C. Yates, S. Lucyszyn, and P. D. Mitcheson, "Maximizing dc-to-load efficiency for inductive power transfer," *IEEE Trans. Power Electron.*, vol. 28, no. 5, pp. 2437–2447, May 2013.
[23] S. I. Babic and C. Akyel, "New analytic-numerical solutions for the mutual inductance of two coaxial circular coils with rectangular cross section in air," *IEEE Trans. Magn.*, vol. 42, no. 6, pp. 1661–1669, Jun. 2006.
[24] J. D. Jackson, "Energy and self- and mutual inductances," in *Classical Electrodynamics*, 3rd ed. New York, NY, USA: John Wiley & Sons, 1999, pp. 215–216.
[25] R. G. Medhurst, "H. F. resistance and self-capacitance of single-layer solenoids," *Wireless Eng*., vol. 24, pp. 35–43, Feb. 1947.
[26] S. Butterworth, "On the alternating current resistance of solenoidal coils," in *Proc. Roy. Soc. London. Ser. A, Math. Phys. Eng. Sci.*, Dec. 1925, vol. 107, no. 744, pp. 693–715.
[27] C. A. Balanis, "Loop antennas," in *Antenna Theory: Analysis and Design*, 3rd ed. New York, NY, USA: John Wiley & Sons, 2005, pp. 231–246.
[28] S. I. Babic and C. Akyel, "New analytic-numerical solutions for the mutual inductance of two coaxial circular coils with rectangular cross section in air," *IEEE Trans. Magn.*, vol. 42, no. 6, pp. 1661–1669, Jun. 2006.
[29] S. Raju, R. Wu, M. Chan, and C. P. Yue, "Modeling of mutual coupling between planar inductors in wireless power applications," *IEEE Trans. Power Electron.* vol. 29, no. 1, pp. 481–490, Jan. 2014.
[30] W. G. Hurley, M. C. Duffy, J. Zhang, I. Lope, B. Kunz, and W. H. Wölfle, "A unified approach to the calculation of self- and mutual-inductance for coaxial coils in air," *IEEE Trans. Power Electron.*, vol. 30, no. 11, pp. 6155–6162, Nov. 2015.
[31] G. Grandi, M. K. Kazimierczuk, A. Massarini, and U. Reggiani, "Stray capacitances of single-layer solenoid air-core inductors," *IEEE Trans. Ind. Appl.*, vol. 35, no. 5, pp. 1162–1168, Sep./Oct. 1999.
[32] C. Akyel, S. I. Babic, and M. M. Mahmoudi, "Mutual inductance calculation for non-coaxial circular air coils with parallel axes," *Prog. Electromagn. Res.*, vol. 91, pp. 287–301, 2009.
[33] S. I. Babic and C. Akyel, "Calculating mutual inductance between circular coils with inclined axes in air," *IEEE Trans. Magn.*, vol. 44, no. 7, pp. 1743–1750, Jul. 2008.

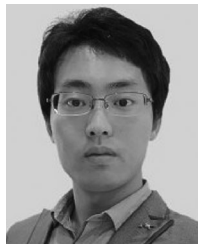

Zixuan Yi was born in Taiyuan, China, in 1991. He received the B.S. degree in electronic engineering and information science from the University of Science and Technology of China, Hefei, China, in 2014, where he is currently working toward the Ph.D. degree in electronic engineering and information science.

His research interests include wireless power transfer systems, microwave passive components, microwave integrated circuits, and antennas.

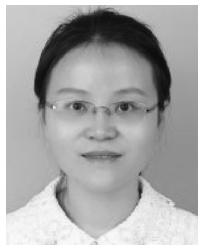

Meiling Li was born in Wuhu, China, in 1988. She received the B.S. degree in electronic information engineering from Anhui University, Hefei, China, in 2010, and the Ph.D. degree in electromagnetism field and microwave technology from the University of Science and Technology of China, Hefei, China, in 2016.

She is currently a postdoctoral researcher with the Department of Electronic Engineering and Information Science, University of Science and Technology of China. Her research interests include wireless power transfer systems, frequency selected surfaces, absorbing materials and structures, and microwave circuits.

Badar Muneer was born in Mirpur Khas, Pakistan, in 1987. He received the B.S., degree in communication systems engineering from the Institute of Space Technology, Islamabad, Pakistan, in 2008, the M.Engg. degree in telecommunication engineering from the NED University of Engineering and Technology, Karachi, Pakistan, in 2012, and the Ph.D. degree in electromagnetism field and microwave technology from the University of Science and Technology of China, Hefei, China.

From 2008 to 2011, he was with a satellite broadcasting company as a Satellite Engineer. From 2016 to 2018, he has been associated with the Chinese Academy of Science under the President's International Fellowship Initiative as a Postdoctoral Fellow. He is currently an Assistant Professor with the Department of Telecommunication Engineering, Mehran University of Engineering and Technology, Jamshoro, Pakistan. His research interests include VSAT, CATV, and many modern broadcast equipment.

Qi Zhu was born in Hefei, China, in 1968. He received the B.S. and M.S. degrees in physics from the Hefei University of Technology, in 1989 and 1992, respectively, and the Ph.D. degree in airplane from the Nanjing University of Aeronautics and Astronautics.

In 1998, he joined the University of Science and Technology of China, Hefei, China as an Associate Professor, and is currently a Professor there. His research interests include microwave and millimeter-wave technology and electromagnetic theory.